Single-Step Synthesis of Dual Phase Bright Blue-Green Emitting Lead Halide Perovskite Nanocrystal Thin Films

Peer-reviewed author version

Bhatia, Harshita; Steele, Julian A.; Martin, Cristina; Keshavarz, Masoumeh; Solis-Fernandez, Guillermo; Yuan, Haifen; Fleury, Guillaume; Huang, Haowei; Dovgaliuk, Iurii; Chernyshov, Dmitry; HENDRIX, Jelle; Roeffaers, Maarten B. J.; Hofkens, Johan & Debroye, Elke (2019) Single-Step Synthesis of Dual Phase Bright Blue-Green Emitting Lead Halide Perovskite Nanocrystal Thin Films. In: CHEMISTRY OF MATERIALS, 31(17), p. 6824-6832.

DOI: 10.1021/acs.chemmater.9b01277
Handle: http://hdl.handle.net/1942/29813

Article

Single-Step Synthesis of Dual Phase Bright Blue-Green Emitting Lead Halide Perovskite Nanocrystal Thin Films

Harshita Bhatia, Julian A. Steele, Cristina Martin, Masoumeh Keshavarz, Guillermo Solis-Fernandez, Haifeng Yuan, Guillaume Fleury, Haowei Huang, Iurii Dovgaliuk, Dmitry Chernyshov, Jelle Hendrix, Maarten B.J. Roeffaers, Johan Hofkens, and Elke Debroye

Chem. Mater., **Just Accepted Manuscript** • DOI: 10.1021/acs.chemmater.9b01277 • Publication Date (Web): 13 Aug 2019

Single-Step Synthesis of Dual Phase Bright Blue-Green Emitting Lead Halide Perovskite Nanocrystal Thin Films

Harshita Bhatia[1], Julian A. Steele[2], Cristina Martin[1,3], Masoumeh Keshavarz[1], Guillermo Solis-Fernandez[1], Haifeng Yuan[1], Guillaume Fleury[2], Haowei Huang[2], Iurii Dovgaliuk[4], Dmitry Chernyshov[4], Jelle Hendrix[1,5], Maarten B.J. Roeffaers[2], Johan Hofkens[1*], Elke Debroye[1*]

1 Department of Chemistry, KU Leuven, Celestijnenlaan 200F, B-3001 Leuven, Belgium

2 Department of Microbial and Molecular Systems, Centre for Surface Chemistry and Catalysis, KU Leuven, B-3001 Leuven, Belgium

3 Departamento de Química Física, Facultad de Farmacia, Universidad de Castilla-La Mancha, 02071 Albacete, Spain

4 Swiss-Norwegian Beamlines at the European Synchrotron Radiation Facility, 71 avenue des Martyrs, F-38000 Grenoble, France

5 Dynamic Bioimaging Lab, Advanced Optical Microscopy Centre and Biomedical Research Institute, Hasselt University, Agoralaan C (BIOMED), B-3590 Diepenbeek

ABSTRACT: Metal trihalide perovskites are rapidly redefining the landscape of solid-state semiconductors utilized as active medium in photovoltaics and in light generation. Within this materials space, organic-inorganic hybrid formamidinium lead bromide ($FAPbBr_3$) has arisen as a promising candidate for efferent light emitting devices, due to its capacity for sharp and bright green light emissions (530 nm). Herein we have applied a facile single-step ligand-mediated method for phase-controlled synthesis of $FAPbBr_3$ cube- and rod-shaped nanocrystals (NCs), starting from different ratios of precursor agents. Examining their structural and optoelectronic properties – using a combination of synchrotron X-ray diffraction, X-ray spectroscopy, scanning electron microscopy and steady-state and time-resolved photoluminescence (PL) – we reveal the two NC types to fundamentally differ. While the cube-shaped NCs exhibit properties aligning with that of bulk $FAPbBr_3$, the nanorods exhibit a two-phase microstructure and the co-existence of both a typical cubic perovskite structure alongside the formation of a new low-symmetry monoclinic phase (P2/m). Further, the two-phase nanorods display a bright dual PL emission (peaks centered near 490 nm and 530 nm) and complex luminescence dynamics, properties characteristic of quasi-2D perovskites. The two phase nanorods generation can be assigned to the proton exchange in the presence of excess of FA^+ during the synthesis.

Very few materials within optoelectronics research have garnered the scientific and technological interest generated by organic-inorganic hybrid perovskite semiconductors – possessing the general ABX_3 chemical formula.[1,2] This recent spike in attention for trihalide perovskite is owed to their unique and interesting combination of optoelectronic properties; from high absorption coefficients and long exciton diffusion lengths (100-1000 nm), to small exciton binding energies and high quantum yields.[3] Further, their tunable emission retains extremely high color purity, all while being solution processable. Needless to say, these properties combine to lay a promising path toward high performance and low-cost light emitting diodes (LEDs).[4–6]

Even though various perovskite systems have shown photoluminescence quantum yields (PLQYs) up to 90% at 450 nm,[7,8] producing color stable and efficient blue LEDs remains challenging.[9–12] Another critical issue is the poor stability of perovskite thin films in LED devices.[13,14] Importantly, the application of polycrystalline material should be avoided since it contains a large number of intrinsic defects which are detrimental for the charge carrier dynamics and initiate parasitic non-radiative recombination pathways.[14,15] The PL efficiency can be improved by confining excitons in small nanograins (~100 nm),[4,15] or by making use of quantum dots (< 20 nm) or nanocrystals while simultaneously passivating the surface defects using ligands.[16,17] Recently, a new perovskite material class has emerged, known as quasi-2D perovskites, possessing the merits of both 3D and 2D structures.[18–20] Quasi-2D systems

are formed by incorporating bulky insulating cation spacers into the inorganic sheets of corner sharing octahedra, in which the insulating cation acts as a barrier and the inorganic layer as a well. Therefore, the generated excitons are confined in the natural multiple-quantum well structure, giving rise to superior PL properties than those of 3D counterparts.[21]

In this manuscript, we report on the synthesis of brightly emissive $FAPbBr_3$ nanocrystals (NCs), using a facile and scalable ligand-mediated wet-chemical method under ambient conditions.[22–24] By taking advantage of proton exchange processes between alkylamines during growth, we find that by increasing the molar concentration of FABr relative to that of the $PbBr_2$ precursor (from one to three-fold), the formation of NCs with a rod-like structure is promoted over nanocubes. An extensive photophysical evaluation of the NCs reveals that, unlike the conventional properties of the nanocubes, our nanorods, FA_2PbBr_4-$FAPbBr_3$, thin films exhibit characteristics consentient with recent reports of quasi-2D perovskite systems, displaying a blue-green emission (490 nm; PLQY 32 % at 445 nm), originating from the presence of a relatively exotic monoclinic $FAPbBr_3$ NC phase.

Results and Discussion

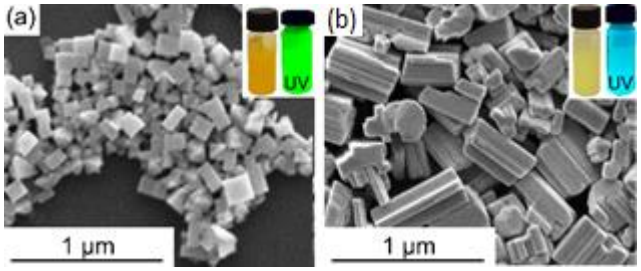

Figure 1. SEM images of (a) $FAPbBr_3$ nanocubes ($PbBr_2$:FABr = 1:1) and (b) $FAPbBr_3$ nanorods ($PbBr_2$:FABr = 1:3) . The insets picture the suspensions under visible (right) and 365 nm UV (left) illumination.

Preparation of NCs

First we outline a new and facile single-step, high yielding route for the synthesis of quasi-2D perovskites. Interestingly, unlike other reported procedures wherein the ammonium cation is intentionally added to obtain the quasi-2D structure,[5,25,26] our synthesis approach induces the formation of an ammonium cation during the synthesis. The preparation steps involve a ligand-mediated wet-chemical approach which is conducted under ambient conditions.[22–24,27] Specifically, by oversaturating the molar concentration of FABr relative to that of the $PbBr_2$ precursor from 1:1 to 3:1, proton exchange between the alkylamines is believed to substantially influence the perovskite formation, i.e. the formed protonated alkylamine capping ligand is found to be integrated into the perovskite lattice. Note that further support and discussion on this process is still to come (vide infra, section XPS, page4). Ultimately, on varying the precursors' molar ratio, colloidal solutions appear distinct in color and possess a substantial difference in size and morphology of the NCs (Figure 1 and S2); green emitting nanocubes (with typical orange color) on the order of 200 nms are formed with a $PbBr_2$: FABr ratio of 1:1, while larger blue emitting nanorods (yellow in color) with dimensions in the order of 400 by 70 nm are formed with a precursor ratio of 1:3. Before characterization, the NCs are transferred from solution onto glass substrates to form stable NC thin films.

Structural Properties

We begin with a structural and compositional overview of the different orange and yellow $FAPbBr_3$ NCs presented in Figure 1. From here on we simply refer to the two NC types based on their differing morphologies, i.e. nanocubes and nanorods, whereby the $FAPbBr_3$ nanocubes will act as an archetypal control to the relatively exotic properties of the nanorods.

EDX compositional analysis:

On the outset, we find that the two NC types differ not only in their color with and without UV excitation (Figure 1), but also in their fundamental compositions. Specifically, surface sensitive EDX analysis (Figure S3) revealed that the nanocubes possess the nominal 1:3 Pb/Br atomic ratio for a 3D metal trihalide perovskite. In contrast, an average atomic ratio of 1:4 is recorded from the nanorods, deviating with a statistical relevance from the nominal 1:3 value seen in the nanocubes. These findings indicate that an excess of FABr induces two distinct phenomena: a transformation in morphology (i.e. cubes to rods) and an increase in Br content relative to Pb. We point out that such compositional deviations are consistent with several recent reports on 2D perovskite systems.[28,29]

Synchrotron X-ray diffraction:

Next we exact the crystal structure and phase purity of the $FAPbBr_3$ NCs using high-resolution XRD. The two NC types were placed in quartz capillaries exposed to a high-

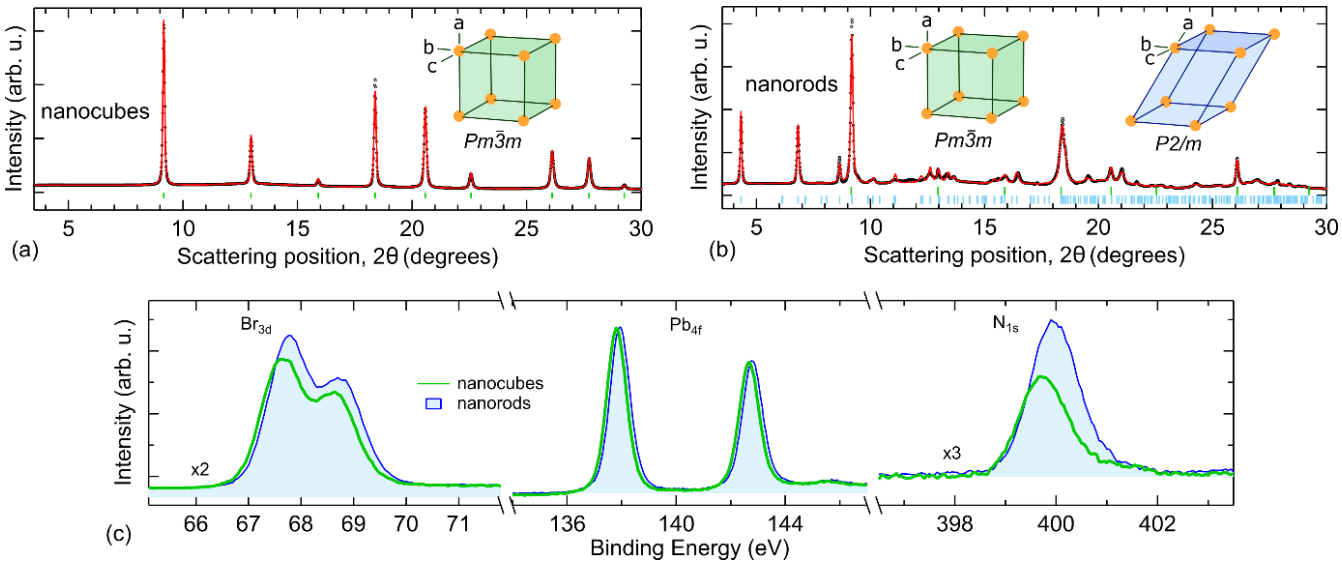

Figure 2. Powder XRD patterns of $FAPbBr_3$ a) nanocubes and b) nanorods (black circles) and their respective refinements (red line). The respective insets show the different unit cells used to generate the refinement, corresponding to the peak positions at the bottom (sticks). (c) XPS spectra expanded over the Br3d, Pb4f and N1s signals for the $FAPbBr_3$ NCs. Both spectra have been normalized to their respective Pb4f peaks (at 137 eV). The peak analysis can be found in Table S1 of SI.

throughput synchrotron X-ray beam tuned to a wavelength of 0.95774 Å, under ambient conditions. Figure 2 presents the respective diffraction scans recorded and the structural refinements made for the two types of NCs. First, in line with the well-known thermodynamically favored structure of $FAPbBr_3$,[30,31] the nanocubes exhibit a cubic structure (refined to a = 5.9943 Å using the $Pm\bar{3}m$ space group) with no obvious reduction in the unit cell translational symmetry.[32] Again, this is in strong contrast to the diffraction pattern recorded for the yellow $FAPbBr_3$ nanorods; here we see the introduction of a large number of additional Bragg peaks, along with a substantial reduction in symmetry, suggested by the extensive splitting of the cubic-like scattering features. A refinement of the XRD data in Figure 2b is best made accounting for two separate phases. Namely, a low-symmetry monoclinic structure (a = 9.0060 Å, b = 8.0570 Å, c = 12.7940 Å and β = 95.40˚using the P2/m space group) is derived from the collection of smaller peaks scattering at both low and high angles, while a smaller contribution from the nominal 3D cubic phase is also present. While the refined XRD scan presented in Figure 2b is quite agreeable to the experimental data, exacting further details is made difficult by the strong presence of a (100) texture (indicative of the rod-shaped morphology), complex organics (i.e. FA), and the two-phase character. To the best of our knowledge, this is the first time that $FAPbBr_3$ has been found to exist in a monoclinic phase. In combination with the compositional difference revealed through the prior EDX data, the monoclinic phase determination can be explained by the formation of a quasi-2D $FAPbBr_3$ structure.[33] The monoclinic cell can be considered as a distorted version of $\sqrt{2}a_c \times \sqrt{2}a_c \times 2a_c$ orthorhombic cell. Such a lattice transformation in perovskites is an indication of a cooperative tilting of $PbBr_6$ octahedra around c-axis; opposite tilting direction for two neighboring layers doubles the c-axis.[34] Notably a and b pseudo-cubic cell dimensions are shorter than c and on average, are practically the same as for the cubic phase (6.364x5.697x6.397, 0.5*(6.364+5.697)=6.03, a_c = 5.9943). We point out that the low-angle monoclinic peaks in Figure 2b do resemble the interplanar scattering peaks seen in true 2D crystal planes,[35] however, such a feature is not necessarily synonymous in a quasi-2D arrangement. The compositional difference revealed through the prior EDX data, agree with the formation of a quasi-2D FAPbBr3 layers.[33] Although, unit cell dimensions clearly indicate that 3D framework of $PbBr_6$ corner-sharing octahedra is preserved.

X-ray photoelectron spectroscopy (XPS):

In the absence of clear low-angle interplanar 2D XRD peaks, we now explore the different coordination details of NCs within the context of the anticipated quasi-2D system (nanorods). Figure 2c presents the X-ray photoelectron spectroscopy (XPS) data recorded from thin films made of the two NCs. First, the spectra acquired from both samples possess consistent chemical features; distinctive peaks of Br3d (~67.5 and 68.5 eV), Pb4f (~137.8 and 142.7 eV) and N1s (~399.8 eV). Carbon peaks were also recorded from these samples, though interpreting their XPS signals is made difficult by the choice of carbon tape sample support. The small difference in peak positions (< 0.2 eV) and widths all fall well within the experimental error of the measurement (induced by crystal charging, etc.), with no notable chemical shifts or

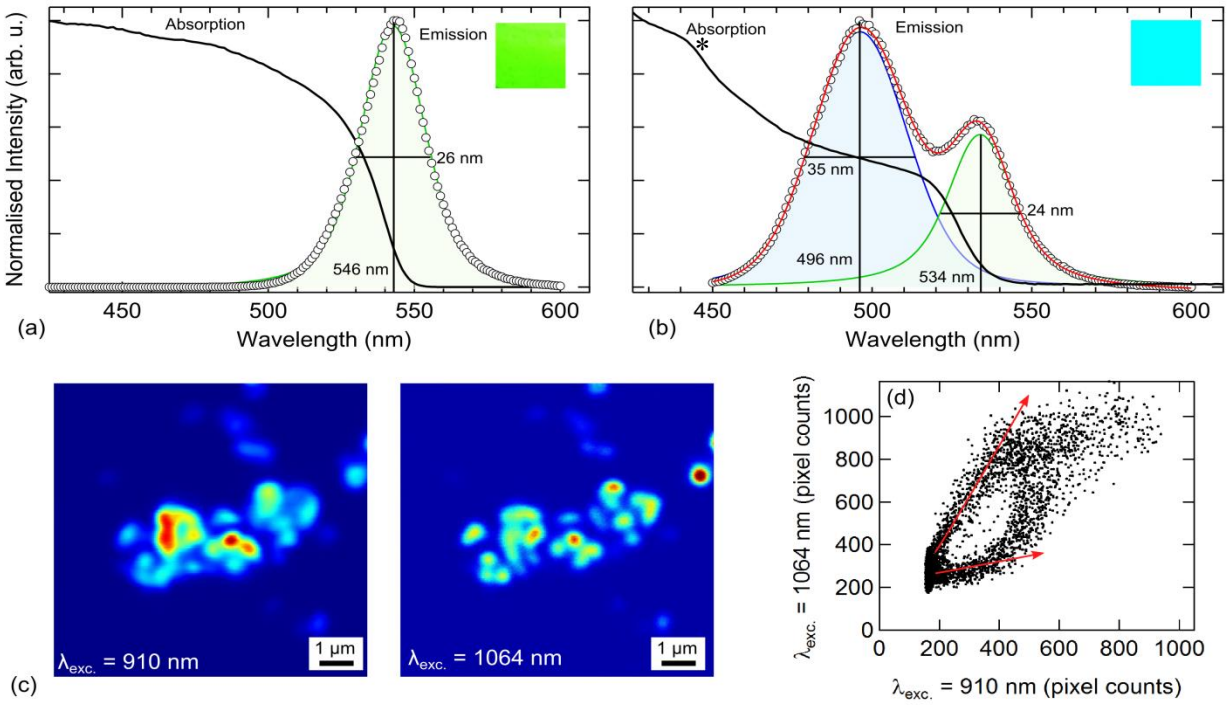

Figure 3. Normalized absorption and emission spectra of dropcasted thin films of FAPbBr3 (a) nanocubes and (b) nanorods, prepared using 1:1 and 1:3 PbBr2/FABr precursor ratio, respectively. For the nanorods, the second high-energy excitonic absorption feature is identified by '*'. The colored squares inset to both plots reflect the difference in perceived PL emission color under a 365 nm UV lamp. (c) Corresponding two-photon PL maps of a collection of FAPbBr3 nanorods, using two 910 nm (left) and 1064 nm (right) photons to excite the emission signals. In both cases, photoluminescence is detected in a reduced spectral window ranging from 495-540 nm, which covers most of the PL emission. (d) Correlation plot of each corresponding map pixels shown in (c), where the red arrows provide a guide for the eye to highlight the anti-correlation.

oxidation states present. Notably in Figure 2c, with both spectra normalized to the Pb4f peak at 137.8 eV there exists a large differencing in the intensity of signal detected from both elements Br and N; in both cases, these signals are relatively stronger with a move to the higher FAPb molar fraction, i.e. the synthesis of quasi-2D nanorods. For completeness, we provide the peak analysis in Table S1 of the SI. This observed rise in the Br signal is consistent with the previous EDX studies, confirming that the Br/Pb ratio in the nanorods increased relative to the nanocubes. We again assign this increase to the highly distorted monoclinic perovskite phase detected through XRD analysis in Figure 2a, and is consentient with the compositional properties commonly observed in 2D perovskite structures; with the formula $(RNH_3)_2PbBr_4$. In addition, the large increase in the N/Pb ratio detected within the XPS signals further supports the notion of excess formamidinium and oleylammonium cations, participating at the quasi-2D perovskite surface.[36–39] Note that the abundance of Br atoms at the perovskite surface is anticipated to play an important role in potentially passivating parasitic surface states.[40]

In the presence of an excess of formamidinium, proton exchange can occur within amine-based systems via homoconjugation (FAH^+···OAm).[41] It follows that oleylamine is transformed into the oleylammonium cation, which competes with FA^+ ions for lattice sites

and promotes the formation of low-dimensional structures represented by the formula $[RNH_3]_2[FAPbBr_3]_{n-1}PbBr_4$.[42,43] As mentioned above, our synthesis approach induces the formation of the ammonium cation during the synthesis. To probe the mechanism involved here, experiments targeting the role of proton excess were carried out. Figure S4 displays the SEM and XRD characterization of materials grown when HBr was added to the synthesis protocol with a $PbBr_2$/FABr 1:1 percursor ratio. In this case, the excess protons provided by the HBr result in the formation of rod-like $FAPbBr_3$ NCs with again the contribution of a monoclinic crystal structure. Therefore, HBr is anticipated to form as an intermediate product during the reaction of $PbBr_2$ with a higher molar concentration of FABr.

Photophysical Properties

Next we evaluate the all-important optical properties of the $FAPbBr_3$ NCs drop-casted in the form of a thin film. Figure 3 shows the steady-state absorption – reflectance spectra converted using the Kubelka-Munk equation $\alpha(R) = (1-R)^2/(2R)$ and PL emission spectra of the $FAPbBr_3$

nanocubes and nanorods. Both samples exhibit a wide absorption band and intense PL emission, however there are several important differences. For the nanocubes, the UV-VIS absorption spectrum in Figure 3a is typical of $FAPbBr_3$, with an absorption onset near 600 nm together with an excitonic feature near 530 nm. The sharp and intense PL emission is also characteristic,[30,44] centered at 546 nm and with a narrow full width at half-maximum (FWHM) of 26 nm, indicative of the high color purity of $FAPbBr_3$, and confirms the overall high quality and uniformity of the nanocubes. Furthermore, the thin film made from the nanocubes is found to remain stable and retain their bright emission, achieving a PL efficiency of 30% at 485 excitation wavelength.

On the other hand, the absorption data recorded from the nanorods contain two clear transition features in Figure 3b, consistent within with a two-phase quasi-2D framework, each having a different electronic structure and bandgap. While the excitonic band at 522 nm is again resolved in the nanorods – characteristic of a 3D $FAPbBr_3$ direct bandgap – an additional blue-shifted excitonic band appears at 440 nm (identified here by '*'). Relative to the nanocubes, the shift in absorption to lower wavelengths in the nanorods specifies its shift in visible color, from orange to yellow, as shown in Figure 1. Although the deformation of a cubic unit cell to a low-symmetry perovskite (like the monoclinic phase revealed here) is typically paralleled by only a minor shift in the electronic bandgap,[40] the blue-shift expressed in our data is inexplicably large and cannot be accounted for based solely on a phase restructuring. Such a strong blue-shift is in agreement with a low-dimensional perovskite structure, consisting of just a few layers of perovskite unit cells[45] and is indicative of quantum confinement.[46] The deconvoluted PL spectrum of the nanorods exhibits a notably more complex emission lineshape than the nanocubes; two relatively narrow PL peaks appear, one centered at 496 nm and another at 530 nm. The low-energy emission corresponds well to the excitonic peak in the absorption spectrum at 520 nm, representing the emission from the 3D portion of the NC composite. Conversely, we assign the high-energy blue emission to radiative recombination originating from the quasi-2D components.[20,45] The thin films made from nanorods exhibited a PLQY up to 19% and 32% at 405 nm and 445 nm excitation, respectively. Interestingly, pumping the cubic phase (λ_{exc} = 485 nm) yielded high PLQY up to 70%, which is comparatively higher than the pure cubic phase. For more details, please refer S6 of SI. However, the quantum yield decreased when exciting further into the band edge since it becomes impossible to record the entire emission range, which partly overlaps with higher excitation wavelengths.

To investigate how the two different emitting species in the quasi-2D conglomerate arrange themselves relative to each other, we first attempted Transmission Electron Microscope (TEM) on these nanorods. However, since the perovskites are very sensitive to high-energy probes, the TEM results were not conclusive. Therefore, we chose to conduct relatively low-energy, two-photon excitation and imaging, on these nanorods, as shown in Figure 3c. Here we have chosen to examine and compare the PL intensity maps recorded consecutively on the same collection of nanorods using both 910 nm and 1064 nm two-photon excitation, corresponding to excitation energies equivalent to 455 nm and 532 nm. In this way, the 910 nm map will consist of an emission comprised of mainly blue (2D) and some green (3D), while the 1064 nm map will only excite the green emitting phase. Thus, if the two separate phases do not coincide in space, there should be an anticorrelation between the corresponding emission maps presented in Figure 3c; i.e. a region which is brighter under one excitation wavelength should be relatively weaker under the other. It follows that evaluating the intensities of corresponding pixels forming the two-photon PL maps (Figure 3d), there exists a strong void where a correlation would exists (i.e. if all points in space were to emit equivalently), and we see instead clear evidence for anticorrelation. At least on the scale of this optical diffraction limited images, the existence and separating distance of the two phases making up the nanorods can be resolved, confirming the quasi-2D microstructure separation of the different phases revealed through both our XRD refinement and optical absorption/emission studies.

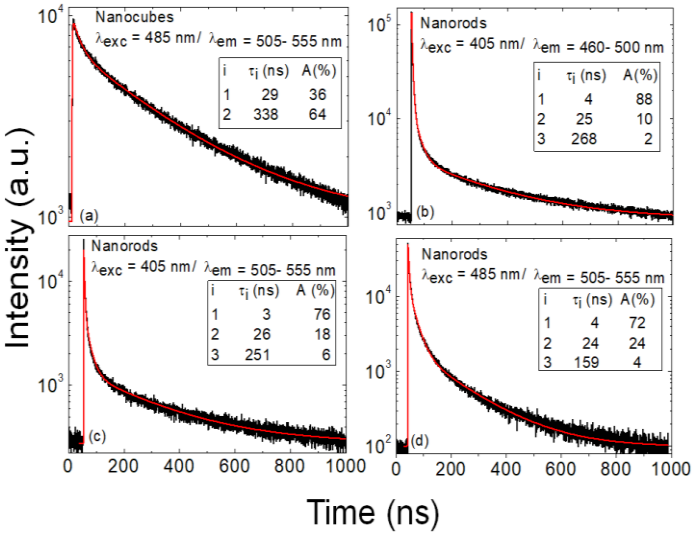

Figure 4. Fluorescence lifetime over the first microsecond for (a) $FAPbBr_3$ nanocubes and (b)-(d) nanorods, with the experimental details and fitting (red line) parameters displayed in the insets.

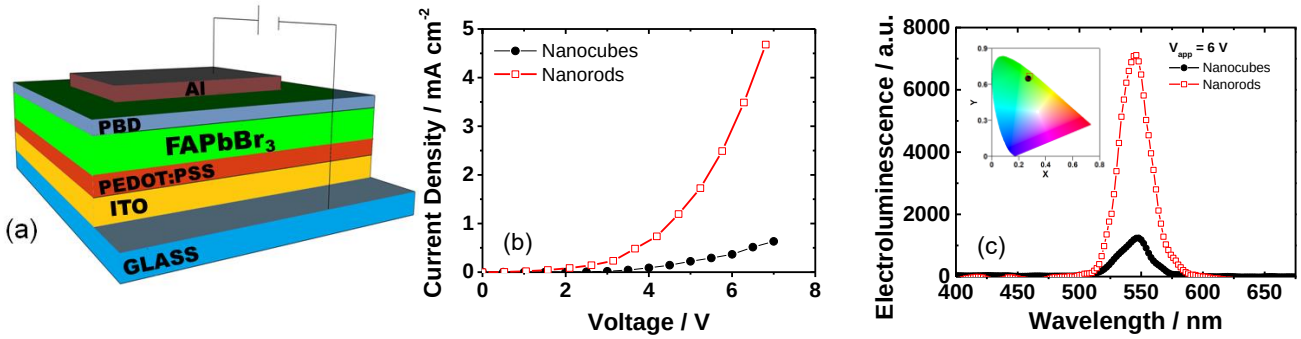

Figure 5. a) PeLED configuration for comparison of the b) I-V response curve for the $FAPbBr_3$ $PbBr_2$/FABr 1:1 nanocubes (black dots) and 1:3 nanorods (red squares) and c) normalized electroluminescence spectra of the hybrid multilayer devices upon 6 V voltage supply. The inset in panel c) displays the CIE coordinates of the electroluminescence at 6 V.

However, resolving phases as well as the ratio of the phases within one crystal is impossible due to diffraction limit of this technique. Furthermore, we executed an excitation power dependence study on potential structural changes and also investigated the influence of excitation power on the growth of the green-emitting phase as well as the stability of nanorods. Please refer to SI (Figure S7 and S8) for more details on this experiment.

PL lifetime measurements:

In evaluating the kinetics of photogenerated charges within our NC thin films, we next investigate the nature of radiative recombination via fluorescence lifetime imaging of an ensemble of NCs. Due to the significant overlap in the two emission bands arising from our quasi-2D nanorods, clean deconvolution of the decaying species is difficult. By assessing the decaying PL signals near each emission wavelength maxima, i.e. at 490 nm and at 530 nm, we can make a qualitative evaluation of the charge dynamic in the two-phase nanorods. Typical PL decays are presented in Figure 4 and their temporal intensities, I(t), were analyzed using either a bi- or tri-exponential fit: $I(t) = \sum_{i=1}^{3} A_i \exp\left(\frac{-t}{\tau_i}\right)$. Here τ_i represent the different lifetime components in order of an increasing time constant, corresponding with a decay amplitude A_i. Further, the lifetime data were recorded through imaging an ensemble of NCs (~20 x 20 µm), forming the basis of the averaged lifetime and amplitude values inset into Figure 4. Generally, the PL emission in perovskites can be described using a simple three-charge recombination pathway model (approximately on three different time scales): (i) fast recombination of bound excitons, or trap-assisted recombination (1-10 ns), (ii) recombination of unbounded excitons (10 – 100 ns), and (iii) clean band-to-band recombination of free charge carriers (100s of ns). Photo-exciting a perovskite crystal, these three processes are observed simultaneously in the PL decay and appropriately fit with three different characteristic exponential components. Among the decaying species, the recombination of excitons typically occurs fastest, and free carrier recombination takes place on much longer time scales – free electrons and holes will scatter though the crystal[47] and will potentially transfer across interfacing phases, to only recombine once they overlap. First, exciting the $FAPbBr_3$ nanocubes in Figure 4a with 485 nm light, two decaying species govern the detected emission at 545 nm; an average fast recombination of 29 ns and an average long component of 338 ns (Table S2). Conversely, for the $FAPbBr_3$ nanorods, three measurement schemes were targeted for comparison; excitation far above the two absorption edges (405 nm) to examine both the blue (Figure 4b) and green (Figure 4c) emitting species, and exciting close to the 3D absorption edge (485) nm) to understand the decay dynamics of the green emission. Overviewing the various decay components of the nanorods, we find that all three are well-described by tri-exponential fits. For all datasets, the decay rate is dominated by the fast component (~ 79 %), indicating a quantum confined quasi-2D system. Typically, for a pure $(OAm)_2PbBr_4$ system, we obtained a monoexponential decay of 2.5 ns. (Figure S5d) This is unsurprising given the general constraints of excitonic recombination within a quantum confined system. Hence, we assign this fast decay to the quasi-2D component in the nanorods (Figure 4b). Interestingly, for the green emitting portion of the nanorods, two long decay components appear again. On exciting the two-phase material with 405 nm light, we imply an interplay of two different processes; i) direct excitation of green emitting species, ii) a substantial portion of excited carriers migrates from the crystal constituent with a wide bandgap to the other with more narrow bandgap. (Figure 4c) As previously stated, this notion has been repeatedly observed in quasi-2D perovskite systems.[48,49] On the other hand, moving to 485 nm excitation causes the long component of the green emission to dramatically shorten to just over 159 ns (Figure 4d and Table S2). This lifetime is substantially shorter than the longest component of the green emission originating from a pure cubic structure (Figure 4a and b). Furthermore, at 485 nm excitation wavelength, the emission contribution is mostly from the 3D perovskites, however, as we also excite the tail end of the quasi-2D blue emissive part, the fast decay component also contributes to the lifetime decay. As mentioned before, the XRD and

PL data confirmed the dual phase nature of rods, which indicates lower crystal purity when compared to the common cubic phase, presumably leading to the faster decay. Lifetime measurements on single rods were not recorded owning to the long decay times observed and the subsequent low photon counts. A more detailed study on the complex decay behavior of the system is on the way.

LED fabrication and characterization:

Based on the good optoelectronic properties described in the previous sections, the application of cube- and rod-shaped $FAPbBr_3$ NCs was tested in light emitting diode (LED) devices in order to unravel the effect of the morphology in the device performance. This type of perovskite material presents its valance band and conduction band around ~ 3,4 and 5.6 eV, respectively,[50,51] which is a good approximation for the energy levels and electrodes selection when designing our device. Therefore, a double layer LED was fabricated using the following configuration: ITO anode/PEDOT:PSS (40 nm)/25 wt% of the $FAPbBr_3$ NCs in a toluene (220 nm)/p-PBD (20 nm)|Al (150 nm). All the layers were spincoated, besides the Al metal cathode (150 nm) which was thermally evaporated. (Figure 5a) The reason for using p-PBD is to improve the electron injection into the perovskite emissive layer and at the same time to inhibit the direct interaction between the Al metal and the perovskite material, which in many cases degrades the perovskite.[52] Please note that currently, we did not optimize the thin film quality of these perovskites as the application is presented just as a proof-of-principle study. Nevertheless, the uniformity of the applied perovskite thin film layer was measured using a non-contact optical profilometer and the results are depicted in Figure S10. Figure 5b shows the current-voltage *I–V* curve for the $PbBr_2$/FABr 1:1 nanocubes and 1:3 nanorods devices, where in both cases, a typical diode characteristic was obtained.[53] Both morphologies exhibit a comparable turn-on voltage of around ~2.8 V. However, it is worth to note that the current density for the nanorods is enhanced by 7 fold at the same bias. This observation suggests that the $FAPbBr_3$ nanorods exhibit better charge injection or mobility properties than the $FAPbBr_3$ nanocubes. To obtain further insights on the optoelectronic properties, the electroluminescence (EL) spectra were recorded (Figure 5c). As it is shown in the CIE coordinates ((0.27, 0.65) and (0.28, 0.67) for nanocubes and nanorods, respectively), the EL spectra features for both samples are nearly identical. However, the EL intensity for the monoclinic nanorods is increased by a factor of 6 under the same bias (6 V). This fact confirms that the charge transport and mobility are improved by modifying the $FAPbBr_3$ crystal structure and morphology. Interestingly, the green EL for cubes (λ_{max} = 547 nm, FWHM = 28 nm) perfectly matches its corresponding PL spectrum (Figure 4), while only the green emission component is contained in the EL spectrum of the nanorods (λ_{max} = 545 nm, FWHM = 27 nm). This has been shown in previous studies and could be a consequence of either a) a higher charge injection and/or more balanced transport into the 3D phase component[54], b) a substantial contribution of radiative recombination of charges in the smallest band gap 3D phase[11] or c) the instability of the lower dimensional phase under heating or moist conditions.

The exact mechanism is still unknown and requires further investigation. Additionally, further steps to stabilize the monoclinic structure of $FAPbBr_3$ perovskites are necessary to improve the device stability and performance.

Conclusion

We demonstrated a facile and scalable method to prepare $FAPbBr_3$ NCs having different morphologies and physicochemical properties by compositional engineering. By applying a three-fold higher molar ratio of FABr, $FAPbBr_3$ nanorods were formed, exhibiting a hybrid quasi-2D perovskite structure. For the first time, a monoclinic phase was observed for this type of FAPbBr3 nanorods. The additional quasi-2D component significantly improved the PLQY from 30 to 70%. The high PLQY value could be attributed to (i) the existence of $FAPbBr_3$ perovskite in the monoclinic phase, (ii) the quasi-2D/3D quantum well-like band alignment in the crystal structure or (iii) the excess of bromide atoms exhibiting a passivating effect to the surface defects. Furthermore, this study reveals a unique mechanism to synthesize a quasi-2D perovskite structure. The presence of a lower dimensional layer containing OAmBr in the nanorods prepared by a 1:3 $PbBr_2$/FABr precursor ratio was further confirmed by XRD, EDX, XPS, and time-resolved PL microscopy. Finally, LEDs were fabricated to investigate the potential application of these NCs in optoelectronic devices. Both types of perovskites nanocrystals exhibited a comparable performance when employed as an emissive layer in LEDs. However, due to the exotic nature of the two–phase system, the impact of different morphologies on the device performance still remains elusive. This work offers new opportunities to study the unexplored monoclinic phase of $FAPbBr_3$ NCs and resolve important questions concerning the charge dynamics within the novel two-phase systems.

Methods

1. Experimental procedure

For the synthesis of FAPbBr3, a precursor solution consisting of 0.02 mmol PbBr2 and 0.02 mmol or 0.06 mmol FABr (1:1 and 1:3 precursor ratios respectively) dissolved in 1 ml of N-dimethylformamide (DMF) was injected dropwise into a vigorously stirring toluene solution, containing oleylamine (OAm) and oleic acid (OAc) as capping ligands. To ensure colloidal stability, the concentration of OAc was fixed to 0.2 mmol. 0.02 mmol and 0.04 mmol of OAm was added for the 1:1 and 1:3 PbBr2/FAbr precursor ratios respectively, as these concentrations yielded the most homo-

geneous NC morphology. After injection, highly luminescent NCs were rapidly formed and to further promote the precipitation/crystal growth, an extra volume of toluene was subsequently added to the suspension. The resulting NCs were centrifuged at 3200 rpm for 15 minutes and washed with toluene to remove the excess of capping agents and unreacted precursor. Finally, they were redispersed in toluene forming a stable colloidal solution. Please refer to the experimental section in the Supporting Information for schematic representation of the synthesis procedure. (Figure S1)

2. Instruments

2.1 Scanning Electron Microscope (SEM): Morphology and composition analysis were studied using FEI Quanta FEG-250 environmental scanning electron microscope at 10 KV, equipped with an energy-dispersive spectrometer. The nanoparticles suspension was drop-casted on a silicon chip prior to the measurement.

2.2 Synchrotron X-Ray Diffraction: Synchrotron-based X-ray diffraction data were collected at BM01 (SNBL/ESRF in Grenoble, France) using PILATUS@SNBL diffractometer.[55] The monochromatic beam (λ = 0.95774 Å) and the parameters of the detector were calibrated on LaB6 powder using PyFAI.[56] The obtained calibrations were implemented to Bubble for further azimuthal integration of 2D images. The resulting unit cell models were refined using the Le Bail method in Fullprof.[57]

2.3 UV-Vis Diffuse reflectance Spectroscopy: Diffuse reflectance spectra (DRS) were recorded on a Perkin Elmer Lambda 950 UV-VIS-NIR spectrophotometer with the 150mm integrating sphere accessory in the wavelength range between 300 nm to 600 nm. The diffuse reflectance (R) data were converted to F(R) using the Kubelka-Monk function: F(R) = (1-R)2/(2R).

2.4 Emission and Excitation Spectroscopy: Excitation and emission spectra were recorded on an Edinburgh Instruments FLS 980 spectrofluorimeter. Samples were measured in front-face mode as thin films created by dropcasting a suspension onto a glass slide that fitted into the Edinburgh solids accessory.

2.5 Photoluminescence quantum yield: Quantum yield measurements were performed on a Horiba Fluorolog 3.22 spectrofluorimeter with F-3029 integrating sphere accessory fitted with a sample holder to accommodate thin film samples drop-casted on a glass slide.

2.6 Two-photon Microscopy: The photoluminescence maps were recorded on an upright microscope (BX61WI/FV1000, Olympus) with 25×, 1.05 NA water immersion objective (XLPLAN, Olympus) using picosecond pulsed lasers of 1064 nm (picoTRAIN, High-Q) and 910 nm (Levante Emerald, APE-Berlin; optical parametric oscillator synchronously pumped by the second harmonic of the Nd:YVO_4 picoTRAIN laser) as excitation sources. The power of each beam at focus was 15 mW. For both excitation sources, the photoluminescence was detected in the epi-direction and transmitted through a 495-540 nm band pass filter before reaching a photomultiplier tuber. The optical resolution of two-photon microscopy can be estimated by the FWHM of the point-spread function, given by equation 1 and 2(for an objective with a numerical aperture superior to 0.7):

$$r_{xy} = \frac{0.325\lambda}{\sqrt{2}NA^{0.91}} 2\sqrt{\ln(2)} \quad (1)$$

$$r_z = \frac{0.532\lambda}{\sqrt{2}} \left[\frac{1}{n-\sqrt{n^2-NA^2}}\right] 2\sqrt{\ln(2)} \quad (2)$$

Where λ is the excitation wavelength, n is the refractive index of the immersion medium, and NA is the numerical aperture of the objective. Thus, as we used 910 nm and 1064 nm as the two excitation sources, the resolution for the two images are respectively given by:

$$r_{xy,910} = 0.316\ \mu m\ ;\ r_{z,910} = 1.102\ \mu m$$

$$r_{xy,1064} = 0.369\ \mu m\ ;\ r_{z,1064} = 1.289\ \mu m$$

2.7 PL Lifetime spectroscopy: Fluorescence lifetime data were recorded on a home-built confocal FLIM microscope. Emission from a pulsed 405-nm laser diode (LDH-P-C-405, Picoquant, Berlin, Germany) was cleaned up spectrally (Semrock 406/15 Brightline HC (AHF F37-406)). Emission from a pulsed 485-nm laser diode (LDH-D-C-485, Picoquant) was cleaned up spectrally (Chroma ET485/20x, F49-482, AHF Analysentechnik, Tübingen, Germany). Laser pulsing was set to 1 MHz (PDL 828 Sepia2, Picoquant). The laser was coupled into a single-mode polarization maintaining optical fiber (PMC-400Si-2.6-NA012-3-APB-150-P, Schäfter+Kirchhoff GmbH, Hamburg, Germany) using a 60FC-4-RGBV11-47 fiber coupler (SuK). Light was collimated using a collimator with xyz adjustable lens (60FC-L-4-RGBV11-47, SuK), the linear polarization cleaned up (CCM1-PBS251, Thorlabs GmbH, Dachau, Germany) and light was reflected via a 3-mm thick polychroic mirror (Chroma zt405/488/561/640rpc, F73-410, AHF) into a galvanometric mirror scanner (TILL Yanus IV digital scanner, FEI Munich, Gräfelfing, Germany) that was connected to the back port of the microscope body (IX71, Olympus Belgium, Berchem Belgium). Imaging was controlled via a home-written software (C#, Microsoft Visual Studio®). Inside the microscope body the light was reflected upwards (3-mm thick Full Reflective Ag Mirror, F21-005, AHF, mounted in a TIRF Filter Cube for BX2/IX2, F91-960, AHF) to the objective (UPLSAPO-60XW, Olympus). Sample emission transmitted through the polychroic mirror was focussed through a 50-µm pinhole (P50S, Thorlabs) via an achromatic lens (AC254-150-A-ML, Thorlabs) and collimated again (AC254-50-A-ML, Thorlabs). After collimation, the emission was reflected on a dichroic mirror

(H560LPXR, F48-559, AHF). Then, the emission was spectrally split into two bands via an additional dichroic mirror (H507LPXR, F48-507): the blue part was spectrally filtered through a 450/50 ET Bandpass emission filter (AHF), the green part through a HQ525/50 bandpass filter (Chroma). Emission was focused (AC254-50-A-ML, Thorlabs) on an avalanche photodiode (τ-SPAD, Picoquant). The detector was connected to a time-correlated single photon counting (TCSPC) device (Hydraharp 400, Picoquant) and powered using a power supply (DSN-102, Picoquant). The laser powers used were 0.15, 0.75 and 1.5 nW, measured between the polychroic mirror and the galvo (LabMax Top, Coherent, Santa Clara, California, USA)(about 40% reached the sample), corresponding to 50, 250 and 500 mW/cm2 respectively (taking into account the size of the focal spot and percentage of laser that actually reaches the sample). Data were loaded in the PAM software.[58] (https://pam.readthedocs.io) written in MATLAB (The MathWorks, Eindhoven, The Netherlands). Instrument response functions (IRF) were recorded by removing the emission filter and imaging the reflection of the laser on the coverslip surface. Data were fitted by 2- or 3-component convolution fitting.

ASSOCIATED CONTENT

This material is available free of charge via the Internet at http://pubs.acs.org.

Detailed scheme of synthesis procedure and additional information on results.

Size distribution of cubes and rods.

Elemental composition.

Peak analysis of XPS spectra.

SEM and XRD of $FAPbBr_3$ formed after adding HBr to 1:1 $PbBr_2$/FABr.

SEM, XRD, PL, absorption and lifetime of 2D perovskites (OAm)2PbBr4.

PL, absorption and PLQY of nanorods recorded in different atmospheric conditions.

Two photon excitation: Effect of excitation power on structural changes and stability.

Recombination lifetimes of nanocubes and nanorods.

Thin film morphology of perovskites used as emissive layer in LEDs.

AUTHOR INFORMATION

Corresponding Author

* Email: Elke.debroye@kuleuven.be
* Email: Johan.hofkens@kuleuven.be

ACKNOWLEDGMENT

The authors acknowledge financial support from the Research Foundation - Flanders (FWO Grant numbers G.0B39.15, G.0B49.15, G098319N and ZW15_09-GOH6316), the EC Marie Curie ITN – iSwitch PhD fellowship to H.B. (Grant number 642196), the Research Foundation - Flanders postdoctoral fellowships to J.A.S., C.M., M.K., H.Y. and E.D. (FWO Grant numbers 12Y7218N, 12J1716N, 12Y6418N, 12R8718N and 12O3719N, respectively), the Research Foundation - Flanders PhD fellowship to G.S.F. (FWO Grant number 1193818N), the KU Leuven Research Fund (C14/15/053), the Flemish government through long term structural funding Methusalem (CASAS2, Meth/15/04) and the Hercules foundation (HER/11/14). J.A.S. and H.Y. acknowledge the XRD support provided by Vadim Diadkin on BM01 at the ESRF.

REFERENCES

(1) Murali, B.; Yengel, E.; Yang, C.; Peng, W.; Alarousu, E.; Bakr, O. M.; Mohammed, O. F. The Surface of Hybrid Perovskite Crystals: A Boon or Bane. *ACS Energy Letters* **2017**, *2* (4), 846–856.

(2) Jeon, N. J.; Noh, J. H.; Yang, W. S.; Kim, Y. C.; Ryu, S.; Seo, J.; Seok, S. I. Compositional Engineering of Perovskite Materials for High-Performance Solar Cells. *Nature* **2015**, *517* (7535), 476–480.

(3) Kim, Y.-H.; Cho, H.; Heo, J. H.; Kim, T.-S.; Myoung, N.; Lee, C.-L.; Im, S. H.; Lee, T.-W. Multicolored Organic/Inorganic Hybrid Perovskite Light-Emitting Diodes. *Advanced Materials* **2015**, *27* (7), 1248–1254.

(4) Cho, H.; Jeong, S.-H.; Park, M.-H.; Kim, Y.-H.; Wolf, C.; Lee, C.-L.; Heo, J. H.; Sadhanala, A.; Myoung, N.; Yoo, S.; et al. Overcoming the Electroluminescence Efficiency Limitations of Perovskite Light-Emitting Diodes. *Science* **2015**, *350* (6265), 1222–1225.

(5) Tan, Z.-K.; Moghaddam, R. S.; Lai, M. L.; Docampo, P.; Higler, R.; Deschler, F.; Price, M.; Sadhanala, A.; Pazos, L. M.; Credgington, D.; et al. Bright Light-Emitting Diodes Based on Organometal Halide Perovskite. *Nature Nanotechnology* **2014**, *9* (9), 687–692.

(6) Zhao, Y.; Zhu, K. Organic–Inorganic Hybrid Lead Halide Perovskites for Optoelectronic and Electronic Applications. *Chemical Society Reviews* **2016**, *45* (3), 655–689.

(7) Huang, H.; Zhao, F.; Liu, L.; Zhang, F.; Wu, X.; Shi, L.; Zou, B.; Pei, Q.; Zhong, H. Emulsion Synthesis of Size-Tunable CH3NH3PbBr3 Quantum Dots: An Alternative Route toward Efficient Light-Emitting Diodes. *ACS Appl. Mater. Interfaces* **2015**, *7* (51), 28128–28133.

(8) Lee, J.-W.; Choi, Y. J.; Yang, J.-M.; Ham, S.; Jeon, S. K.; Lee, J. Y.; Song, Y.-H.; Ji, E. K.; Yoon, D.-H.; Seo, S.; et al. *In-Situ* Formed Type I Nanocrystalline Perovskite Film for Highly Efficient Light-Emitting Diode. *ACS Nano* **2017**, *11* (3), 3311–3319.

(9) Bohn, B. J.; Tong, Y.; Gramlich, M.; Lai, M. L.; Döblinger, M.; Wang, K.; Hoye, R. L. Z.; Müller-Buschbaum, P.; Stranks, S. D.; Urban, A. S.; et al. Boosting Tunable Blue Luminescence of Halide Perovskite Nanoplatelets through Postsynthetic Surface Trap Repair. *Nano Lett.* **2018**, *18* (8), 5231–5238.

(10) Lignos, I.; Protesescu, L.; Emiroglu, D. B.; Maceiczyk, R.; Schneider, S.; Kovalenko, M. V.; deMello, A. J. Unveiling the Shape Evolution and Halide-Ion-Segregation in Blue-Emitting Formamidinium Lead Halide Perovskite Nanocrystals Using an Automated Microfluidic Platform. *Nano Lett.* **2018**, *18* (2), 1246–1252.

(11) Yang, X.; Zhang, X.; Deng, J.; Chu, Z.; Jiang, Q.; Meng, J.; Wang, P.; Zhang, L.; Yin, Z.; You, J. Efficient Green Light-Emitting Diodes Based on Quasi-Two-Dimensional Composition and Phase Engineered Perovskite with Surface Passivation. *Nature Communications* **2018**, *9* (1).

(12) Kumar, S.; Jagielski, J.; Yakunin, S.; Rice, P.; Chiu, Y.-C.; Wang, M.; Nedelcu, G.; Kim, Y.; Lin, S.; Santos, E. J. G.; et al. Efficient Blue Electroluminescence Using Quantum-Confined Two-Dimensional Perovskites. *ACS Nano* **2016**, *10* (10), 9720–9729.

(13) Li, Z.; Yang, M.; Park, J.-S.; Wei, S.-H.; Berry, J. J.; Zhu, K. Stabilizing Perovskite Structures by Tuning Tolerance Factor:

Formation of Formamidinium and Cesium Lead Iodide Solid-State Alloys. *Chemistry of Materials* **2016**, *28* (1), 284–292.

(14) Yuan, H.; Debroye, E.; Janssen, K.; Naiki, H.; Steuwe, C.; Lu, G.; Moris, M.; Orgiu, E.; Uji-i, H.; De Schryver, F.; et al. Degradation of Methylammonium Lead Iodide Perovskite Structures through Light and Electron Beam Driven Ion Migration. *The Journal of Physical Chemistry Letters* **2016**, *7* (3), 561–566.

(15) Xiao, Z.; Kerner, R. A.; Zhao, L.; Tran, N. L.; Lee, K. M.; Koh, T.-W.; Scholes, G. D.; Rand, B. P. Efficient Perovskite Light-Emitting Diodes Featuring Nanometre-Sized Crystallites. *Nature Photonics* **2017**, *11* (2), 108–115.

(16) Quan, L. N.; Yuan, M.; Comin, R.; Voznyy, O.; Beauregard, E. M.; Hoogland, S.; Buin, A.; Kirmani, A. R.; Zhao, K.; Amassian, A.; et al. Ligand-Stabilized Reduced-Dimensionality Perovskites. *Journal of the American Chemical Society* **2016**, *138* (8), 2649–2655.

(17) Aharon, S.; Etgar, L. Two Dimensional Organometal Halide Perovskite Nanorods with Tunable Optical Properties. *Nano Lett.* **2016**, *16* (5), 3230–3235.

(18) Chen, Y.; Sun, Y.; Peng, J.; Tang, J.; Zheng, K.; Liang, Z. 2D Ruddlesden–Popper Perovskites for Optoelectronics. *Advanced Materials* **2018**, *30* (2), 1703487.

(19) Li, L.; Zhou, N.; Chen, Q.; Shang, Q.; Zhang, Q.; Wang, X.; Zhou, H. Unraveling the Growth of Hierarchical Quasi-2D/3D Perovskite and Carrier Dynamics. *J. Phys. Chem. Lett.* **2018**, *9* (5), 1124–1132.

(20) Byun, J.; Cho, H.; Wolf, C.; Jang, M.; Sadhanala, A.; Friend, R. H.; Yang, H.; Lee, T.-W. Efficient Visible Quasi-2D Perovskite Light-Emitting Diodes. *Advanced Materials* **2016**, *28* (34), 7515–7520.

(21) Wang, Z.; Wang, F.; Sun, W.; Ni, R.; Hu, S.; Liu, J.; Zhang, B.; Alsaed, A.; Hayat, T.; Tan, Z. Manipulating the Trade-off Between Quantum Yield and Electrical Conductivity for High-Brightness Quasi-2D Perovskite Light-Emitting Diodes. *Advanced Functional Materials* **2018**, *28* (47), 1804187.

(22) Zhang, F.; Zhong, H.; Chen, C.; Wu, X.; Hu, X.; Huang, H.; Han, J.; Zou, B.; Dong, Y. Brightly Luminescent and Color-Tunable Colloidal $CH_3NH_3PbX_3$ (X = Br, I, Cl) Quantum Dots: Potential Alternatives for Display Technology. *ACS Nano* **2015**, *9* (4), 4533–4542.

(23) Huang, H.; Susha, A. S.; Kershaw, S. V.; Hung, T. F.; Rogach, A. L. Control of Emission Color of High Quantum Yield $CH_3NH_3PbBr_3$ Perovskite Quantum Dots by Precipitation Temperature. *Advanced Science* **2015**, *2* (9), 1500194.

(24) Zhang, F.; Chen, C.; Kershaw, S. V.; Xiao, C.; Han, J.; Zou, B.; Wu, X.; Chang, S.; Dong, Y.; Rogach, A. L.; et al. Ligand-Controlled Formation and Photoluminescence Properties of $CH_3NH_3PbBr_3$ Nanocubes and Nanowires. *ChemNanoMat* **2017**, *3* (5), 303–310.

(25) Quan, L. N.; Zhao, Y.; García de Arquer, F. P.; Sabatini, R.; Walters, G.; Voznyy, O.; Comin, R.; Li, Y.; Fan, J. Z.; Tan, H.; et al. Tailoring the Energy Landscape in Quasi-2D Halide Perovskites Enables Efficient Green-Light Emission. *Nano Letters* **2017**, *17* (6), 3701–3709.

(26) Bhaumik, S.; Veldhuis, S. A.; Ng, Y. F.; Li, M.; Muduli, S. K.; Sum, T. C.; Damodaran, B.; Mhaisalkar, S.; Mathews, N. Highly Stable, Luminescent Core–Shell Type Methylammonium–Octylammonium Lead Bromide Layered Perovskite Nanoparticles. *Chem. Commun.* **2016**, *52* (44), 7118–7121.

(27) Debroye, E.; Yuan, H.; Bladt, E.; Baekelant, W.; Van der Auweraer, M.; Hofkens, J.; Bals, S.; Roeffaers, M. B. J. Facile Morphology-Controlled Synthesis of Organolead Iodide Perovskite Nanocrystals Using Binary Capping Agents. *ChemNanoMat* **2017**, *3* (4), 223–227.

(28) Vassilakopoulou, A.; Papadatos, D.; Zakouras, I.; Koutselas, I. Mixtures of Quasi-Two and Three Dimensional Hybrid Organic-Inorganic Semiconducting Perovskites for Single Layer LED. *Journal of Alloys and Compounds* **2017**, *692*, 589–598.

(29) Vassilakopoulou, A.; Papadatos, D.; Koutselas, I. Room Temperature Light Emitting Diode Based on 2D Hybrid Organic-Inorganic Low Dimensional Perovskite Semiconductor. *Applied Materials Today* **2016**, *5*, 128–133.

(30) Hanusch, F. C.; Wiesenmayer, E.; Mankel, E.; Binek, A.; Angloher, P.; Fraunhofer, C.; Giesbrecht, N.; Feckl, J. M.; Jaegermann, W.; Johrendt, D.; et al. Efficient Planar Heterojunction Perovskite Solar Cells Based on Formamidinium Lead Bromide. *The Journal of Physical Chemistry Letters* **2014**, *5* (16), 2791–2795.

(31) Noh, J. H.; Im, S. H.; Heo, J. H.; Mandal, T. N.; Seok, S. I. Chemical Management for Colorful, Efficient, and Stable Inorganic–Organic Hybrid Nanostructured Solar Cells. *Nano Letters* **2013**, *13* (4), 1764–1769.

(32) Carpenter, M. A.; Howard, C. J. Symmetry Rules and Strain/Order-Parameter Relationships for Coupling between Octahedral Tilting and Cooperative Jahn–Teller Transitions in ABX3 Perovskites. I. Theory. *Acta Cryst B* **2009**, *65* (2), 134–146.

(33) Safdari, M.; H. Svensson, P.; Tam Hoang, M.; Oh, I.; Kloo, L.; M. Gardner, J. Layered 2D Alkyldiammonium Lead Iodide Perovskites: Synthesis, Characterization, and Use in Solar Cells. *Journal of Materials Chemistry A* **2016**, *4* (40), 15638–15646.

(34) Glazer, A. M. The Classification of Tilted Octahedra in Perovskites. *Acta Crystallographica Section B Structural Crystallography and Crystal Chemistry* **1972**, *28* (11), 3384–3392.

(35) Weidman, M. C.; Seitz, M.; Stranks, S. D.; Tisdale, W. A. Highly Tunable Colloidal Perovskite Nanoplatelets through Variable Cation, Metal, and Halide Composition. *ACS Nano* **2016**, *10* (8), 7830–7839.

(36) Kim, Y.-H.; Lee, G.-H.; Kim, Y.-T.; Wolf, C.; Yun, H. J.; Kwon, W.; Park, C. G.; Lee, T.-W. High Efficiency Perovskite Light-Emitting Diodes of Ligand-Engineered Colloidal Formamidinium Lead Bromide Nanoparticles. *Nano Energy* **2017**, *38*, 51–58.

(37) Milosavljević, A. R.; Huang, W.; Sadhu, S.; Ptasinska, S. Low-Energy Electron-Induced Transformations in Organolead Halide Perovskite. *Angewandte Chemie International Edition* **2016**, *55* (34), 10083–10087.

(38) Zhang, Y.; Wang, C.; Deng, Z. Colloidal Synthesis of Monolayer-Thick Formamidinium Lead Bromide Perovskite Nanosheets with a Lateral Size of Micrometers. *Chemical Communications* **2018**, *54* (32), 4021–4024.

(39) Huang, W.; Manser, J. S.; Sadhu, S.; Kamat, P. V.; Ptasinska, S. Direct Observation of Reversible Transformation of $CH_3NH_3PbI_3$ and NH_4PbI_3 Induced by Polar Gaseous Molecules. *J. Phys. Chem. Lett.* **2016**, *7* (24), 5068–5073.

(40) Li, X.; Wu, Y.; Zhang, S.; Cai, B.; Gu, Y.; Song, J.; Zeng, H. $CsPbX_3$ Quantum Dots for Lighting and Displays: Room-Temperature Synthesis, Photoluminescence Superiorities, Underlying Origins and White Light-Emitting Diodes. *Advanced Functional Materials* **2016**, *26* (15), 2435–2445.

(41) Coetzee, J. F.; Padmanabhan, G. R. Properties of Bases in Acetonitrile as Solvent. IV. Proton Acceptor Power and Homoconjugation of Mono- and Diamines. *J. Am. Chem. Soc.* **1965**, *87* (22), 5005–5010.

(42) Weidman, M. C.; Goodman, A. J.; Tisdale, W. A. Colloidal Halide Perovskite Nanoplatelets: An Exciting New Class of Semiconductor Nanomaterials. *Chem. Mater.* **2017**, *29* (12), 5019–5030.

(43) Almeida, G.; Goldoni, L.; Akkerman, Q.; Dang, Z.; Khan, A. H.; Marras, S.; Moreels, I.; Manna, L. Role of Acid–Base Equilibria in the Size, Shape, and Phase Control of Cesium Lead Bromide Nanocrystals. *ACS Nano* **2018**, *12* (2), 1704–1711.

(44) Eperon, G. E.; Stranks, S. D.; Menelaou, C.; Johnston, M. B.; Herz, L. M.; Snaith, H. J. Formamidinium Lead Trihalide: A Broadly Tunable Perovskite for Efficient Planar Heterojunction Solar Cells. *Energy & Environmental Science* **2014**, *7* (3), 982.

(45) US20170321117A1 - Highly tunable colloidal perovskite nanoplatelets - Google Patents https://patents.google.com/patent/US20170321117A1/en (accessed Oct 31, 2018).

(46) Even, J.; Pedesseau, L.; Katan, C. Understanding Quantum Confinement of Charge Carriers in Layered 2D Hybrid Perovskites. *ChemPhysChem* **2014**, *15* (17), 3733–3741.

(47) Shi, D.; Adinolfi, V.; Comin, R.; Yuan, M.; Alarousu, E.; Buin, A.; Chen, Y.; Hoogland, S.; Rothenberger, A.; Katsiev, K.; et al. Low Trap-State Density and Long Carrier Diffusion in Organolead Trihalide Perovskite Single Crystals. *Science* **2015**, *347* (6221), 519–522.

(48) Milot, R. L.; Sutton, R. J.; Eperon, G. E.; Haghighirad, A. A.; Martinez Hardigree, J.; Miranda, L.; Snaith, H. J.; Johnston, M. B.; Herz, L. M. Charge-Carrier Dynamics in 2D Hybrid Metal–Halide Perovskites. *Nano Letters* **2016**, *16* (11), 7001–7007.

(49) Blancon, J.-C.; Tsai, H.; Nie, W.; Stoumpos, C. C.; Pedesseau, L.; Katan, C.; Kepenekian, M.; Soe, C. M. M.; Appavoo, K.; Sfeir, M. Y.; et al. Extremely Efficient Internal Exciton Dissociation through Edge States in Layered 2D Perovskites. *Science* **2017**, *355* (6331), 1288–1292.

(50) Perumal, A.; Shendre, S.; Li, M.; Tay, Y. K. E.; Sharma, V. K.; Chen, S.; Wei, Z.; Liu, Q.; Gao, Y.; Buenconsejo, P. J. S.; et al. High Brightness Formamidinium Lead Bromide Perovskite Nanocrystal Light Emitting Devices. *Scientific Reports* **2016**, *6*, 36733.

(51) Aygüler, M. F.; Weber, M. D.; Puscher, B. M. D.; Medina, D. D.; Docampo, P.; Costa, R. D. Light-Emitting Electrochemical Cells Based on Hybrid Lead Halide Perovskite Nanoparticles. *The Journal of Physical Chemistry C* **2015**, *119* (21), 12047–12054.

(52) Guerrero, A.; You, J.; Aranda, C.; Kang, Y. S.; Garcia-Belmonte, G.; Zhou, H.; Bisquert, J.; Yang, Y. Interfacial Degradation of Planar Lead Halide Perovskite Solar Cells. *ACS Nano* **2016**, 10 (1), 218–224.

(53) Sah, C.; Noyce, R. N.; Shockley, W. Carrier Generation and Recombination in P-N Junctions and P-N Junction Characteristics. *Proceedings of the IRE* **1957**, 45 (9), 1228–1243.

(54) Veldhuis, S. A.; Boix, P. P.; Yantara, N.; Li, M.; Sum, T. C.; Mathews, N.; Mhaisalkar, S. G. Perovskite Materials for Light-Emitting Diodes and Lasers. *Advanced Materials* **2016**, 28 (32), 6804–6834.

(55) Dyadkin, V.; Pattison, P.; Dmitriev, V.; Chernyshov, D. A New Multipurpose Diffractometer PILATUS@SNBL. *Journal of Synchrotron Radiation* **2016**, 23 (3), 825–829.

(56) Ashiotis, G.; Deschildre, A.; Nawaz, Z.; Wright, J. P.; Karkoulis, D.; Picca, F. E.; Kieffer, J. The Fast Azimuthal Integration Python Library: PyFAI. *J Appl Crystallogr* **2015**, 48 (2), 510–519.

(57) Rodríguez-Carvajal, J. Recent Advances in Magnetic Structure Determination by Neutron Powder Diffraction. *Physica B: Condensed Matter* **1993**, 192 (1–2), 55–69.

(58) Schrimpf, W.; Barth, A.; Hendrix, J.; Lamb, D. C. PAM: A Framework for Integrated Analysis of Imaging, Single-Molecule, and Ensemble Fluorescence Data. *Biophysical Journal* **2018**, 114 (7), 1518–1528.

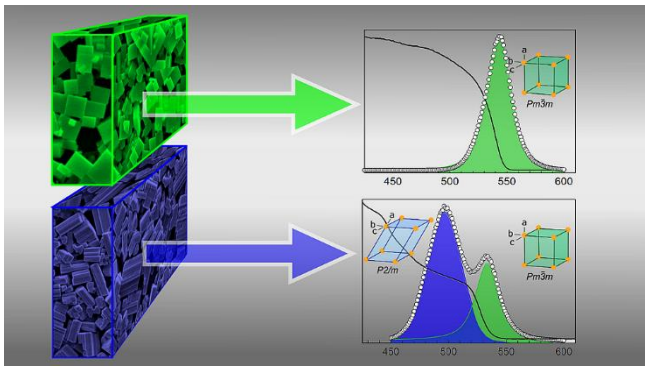
Pm3m
450
500
550
600
P2/m
Pm3m
450
500
550
600